CrossMark

Physical Model of Dust Polarization by Radiative Torque Alignment and Disruption and Implications for Grain Internal Structures

Hyeseung Lee[1], Thiem Hoang[1,2] , Ngan Le[3,4], and Jungyeon Cho[1,5]

[1] Korea Astronomy and Space Science Institute, Daejeon 34055, Republic of Korea; thiemhoang@kasi.re.kr
[2] Korea University of Science and Technology, 217 Gajeong-ro, Yuseong-gu, Daejeon, 34113, Republic of Korea
[3] Institute of Astronomy, Faculty of Physics, Astronomy and Informatics, Nicolaus Copernicus University, Grudziadzka 5, 87-100 Torun, Poland
[4] Department of Space and Applications, University of Science and Technology of Hanoi, Vietnam Academy of Science and Technology, 18 Hoang Quoc Viet, Hanoi, Vietnam
[5] Chungnam National University, Daejeon 34134, Republic of Korea

Abstract

Dust polarization depends on mechanical properties of dust as well as on local environments. To understand how dust polarization varies with different properties, we model the wavelength-dependence polarization of starlight and polarized dust emission of aligned grains by simultaneously taking into account grain alignment and rotational disruption by radiative torques (RATs). We explore a wide range of the local radiation field and grain mechanical properties characterized by tensile strength (S_{max}). We find that the peak wavelength shifts to shorter wavelengths as the radiation strength (U) increases due to the enhanced alignment of small grains. Grain rotational disruption by RATs tends to decrease the optical-NIR polarization but increase the UV polarization of starlight due to the conversion of large grains into smaller ones. In particular, we find that the polarization degree at $850\,\mu m$ (P_{850}) does not increase monotonically with U or grain temperature (T_d), but it depends on S_{max} of the grains. Our model can be tested with observations toward star-forming regions or molecular clouds irradiated by a nearby star, which have higher radiation intensities than the that of the average interstellar radiation field. Finally, we compare our predictions of the P_{850}–T_d relationship with Planck data and find that the observed decrease of P_{850} with T_d can be explained when grain disruption by RATs is accounted for, suggesting that as interstellar grains are unlikely to have a compact structure, perhaps they have a composite one. The variation of the polarization degree with U (or T_d) can provide a valuable constraint on the internal structure of cosmic dust.

Unified Astronomy Thesaurus concepts: Interstellar medium (847); Starlight polarization (1571); Interstellar radiation field (852); Interstellar dust extinction (837)

1. Introduction

Dust is an intrinsic component of the interstellar medium (ISM) and plays important roles in astrophysics. Dust grains absorb and scatter starlight, and infrared emission from heated dust grains is a powerful probe of star and planet formation. The photoelectric effect from small dust grains is essential for the heating and cooling of molecular gas, and grain surfaces are catalytic sites for molecule formation (see Draine 2011).

The polarization of starlight (Hall 1949; Hiltner 1949) and polarized thermal emission (Hildebrand 1989) due to the alignment of dust grains with ambient magnetic fields allow us to map magnetic fields in various environmental conditions (Lazarian 2007), from the diffuse medium to molecular clouds (MCs) to circumstellar regions (see Lai et al. 2003; Crutcher 2012; Andersson 2015). Moreover, polarized thermal emission from aligned grains is a major foreground contamination of cosmic microwave background (CMB) that must be separated to accurately measure the CMB B-modes (Lazarian & Finkbeiner 2003). It is now established that an accurate model of the dust polarization spectrum is required for the precise detection of B-modes (Planck Collaboration et al. 2016). Such an accurate model of dust polarization depends on dust physical properties (size, shape, and composition), grain alignment with magnetic fields, and the gas density and magnetic field structures.

The discovery of starlight polarization shows that interstellar grains are aligned with their long axes perpendicular to the magnetic field. The question of how dust grains become aligned with the magnetic field is a long-standing problem in astrophysics (see Andersson et al. 2015 and Lazarian et al. 2015 for recent reviews). In general, to achieve efficient alignment with the magnetic field, grains must own a magnetic moment and rotate suprathermally, i.e., at velocities above their thermal rotation value (Purcell 1979; Hoang & Lazarian 2016). Rotating paramagnetic grains that contain unpaired electrons (e.g., silicates) are magnetized and, thus, develop a magnetic moment via the Barnett effect (Dolginov & Mitrofanov 1976). Once the grain acquires a magnetic moment, it precesses rapidly about the external magnetic field, which establishes the axis of grain alignment.

After several decades, the radiative torque (RAT) alignment theory became a popular mechanism to explain grain alignment. The idea of RATs was first introduced by Dolginov & Mitrofanov (1976), which were quantified based on differential scattering and absorption of left- and right-handed photons (i.e., photon angular momentum). Numerical calculations for several realistically irregular shapes were carried out by Draine & Weingartner (1996, 1997). However, an analytical model that provides physical insights into RATs and RAT alignment was formulated by Lazarian & Hoang (2007) where RATs were quantified based on the transfer of photon momentum to

the helical grain. Extended numerical calculations of RAT alignment for the different environments were carried out in Hoang & Lazarian (2008, 2009a, 2014). A unified theory of grain alignment for grains with iron inclusions is introduced in Hoang & Lazarian (2016). Recently, numerical calculations of RATs for a large ensemble of grain shapes were presented by Herranen et al. (2019).

One of the key predictions of the RAT alignment theory is that the degree of grain alignment depends on the local conditions, including the radiation field and gas properties (density and temperature) (Lazarian & Hoang 2019). Toward the center of a dense molecular cloud with decreasing radiation intensity, only large grains can be aligned by attenuated interstellar photons (Cho & Lazarian 2005). As a result, the peak wavelength (λ_{max}) of starlight polarization would increase with increasing visual extinction A_V (Lazarian & Hoang 2007; Hoang et al. 2015). This prediction was supported by observational data by Whittet et al. (2008). The angle-dependence of RAT alignment (Hoang & Lazarian 2009b) was also tested by observations of starlight polarization in Andersson et al. (2011). Submillimeter/FIR polarization of starless cores also reveals the existence of a polarization hole (Alves et al. 2014; Jones et al. 2015), which is expected from RAT theory. In the other regime of strong radiation sources, RAT theory predicts an increased alignment of grains when the radiation strength increases, and the peak wavelength is shifted to smaller values. Such a prediction is consistent with some observations toward Type Ia supernovae (SNe Ia; Patat et al. 2015; Zelaya et al. 2017; Hoang 2019a; Giang et al. 2020). Therefore, the polarization degree of polarized emission is expected to increase with increasing radiation intensity according to the classical picture of RAT theory (Lazarian & Hoang 2007).

In addition to grain alignment, the grain size distribution is required for modeling dust emission and the polarization spectrum. The grain size distribution is expected to evolve from the ISM to dense molecular clouds due to various physical effects. For instance, grains can be destroyed via grain shattering as well as thermal and nonthermal sputtering in interstellar shocks (Tielens et al. 1994; Jones et al. 1996). On the other hand, grains can grow in dense molecular clouds due to the accretion of gas species onto the grain surface as well as coagulation due to grain–grain collisions (see Zhukovska et al. 2018 and references therein). In the diffuse medium, grain shattering induced by grain acceleration via magnetohydro-dynamic (MHD) turbulence (Yan et al. 2004; Hoang et al. 2012) is thought to determine the upper cutoff of the grain size distribution (Hirashita & Yan 2009). However, a new physical mechanism, the so-called RAdiative Torque Disruption (RATD), which dominates the upper cutoff of the grain size distribution, was recently discovered by Hoang et al. (2019). This RATD mechanism is based on the fact that suprathermally rotating grains spun-up by RATs induces centrifugal stress that can exceed the maximum tensile strength of grain materials, resulting in the instantaneous disruption of a large grain into small fragments. Since RATs are stronger for larger grains (Lazarian & Hoang 2007; Hoang & Lazarian 2008), RATD is more efficient for large grains than for small ones. As shown in Hoang (2019b), the RATD mechanism is much faster than grain shattering and, thus, determines the upper cutoff of the grain size distribution in the ISM.

According to the RATD mechanism, the upper cutoff of the grain size distribution is determined by tensile strength, which depends on grain internal structure (i.e., compact versus

composite structures; Hoang 2019b). Unfortunately, grain structure is one of the least constrained dust physical properties. In principle, one can constrain the internal structure with observational data if the variation of the polarization with the tensile strength is theoretically predicted (Hoang 2019b). Therefore, the main goal of this paper is first to perform detailed modeling of multiwavelength dust polarization from optical/UV to FIR/submillimeter for different local radiation intensities and grain tensile strengths by simultaneously taking into account the alignment and rotational disruption of grains by RATs.

Full-sky polarization data from Planck have provided invaluable information about dust properties, grain alignment, and magnetic fields. A high polarization degree observed from the diffuse and translucent clouds by Planck reveals that dust grains must be efficiently (perfectly) aligned, which is consistent with a unified alignment theory of grains with iron inclusions (Hoang & Lazarian 2016). However, a detailed analysis of the polarization data for various clouds by Planck Collaboration et al. (2018) shows that the polarization degree at $\lambda = 850\,\mu m$ (P_{850}) does not always increase with grain temperature (T_d) as expected from classical RAT theory. Instead, polarization degree decreases with grain temperature for $T_d \gtrsim 19$ K. This observed feature was thought to be a challenge to the classical picture of RAT alignment theory. However, as we will show in the paper, this unexpected trend would provide a valuable constraint on the tensile strength and then the internal structure of interstellar grains.

The structure of the paper is organized as follows. In Section 2, we describe the RAT alignment and RATD mechanism and our theoretical models. In Sections 3 and 4, we calculate the alignment size, disruption size for the different radiation fields, and present our modeling results of polarized starlight and polarized dust emission. In Section 5, we discuss the implications of our study, focusing on the first constraint of grain internal structure with Planck data and the understanding of anomalous polarization of SNe Ia. A summary of our main findings is presented in Section 6.

2. Grain Alignment and Grain Disruption by Radiative Torques

In this section, we briefly review the theory of grain alignment and rotational disruption by RATs.

2.1. Grain Alignment by RATs

2.1.1. Critical Size of Aligned Grains

Let u_λ be the spectral energy density of some radiation field. The total energy density is $u_{rad} = \int u_\lambda d\lambda$. For the average interstellar radiation field (ISRF) in the solar neighborhood from Mathis et al. (1983), one obtains an energy density $u_{ISRF} = 8.64 \times 10^{-13}$ erg cm^{-3} and a mean wavelength $\bar{\lambda} = 1.2\,\mu m$ (Draine & Weingartner 1997). Assuming that the radiation spectrum u_λ is the same as the ISRF, one can describe the radiation energy density at a given location in the ISM by a dimensionless parameter $U = u_{rad}/u_{ISRF}$, which is referred to as the *radiation strength*.

To account for the variation of the local radiation intensity in the ISM, we will consider a wide range of radiation strength for both the diffuse ISM and a molecular cloud illuminated by a nearby star, as depicted in Figure 1. We assume that a line of sight close to the star probes grains exposed to an averaged
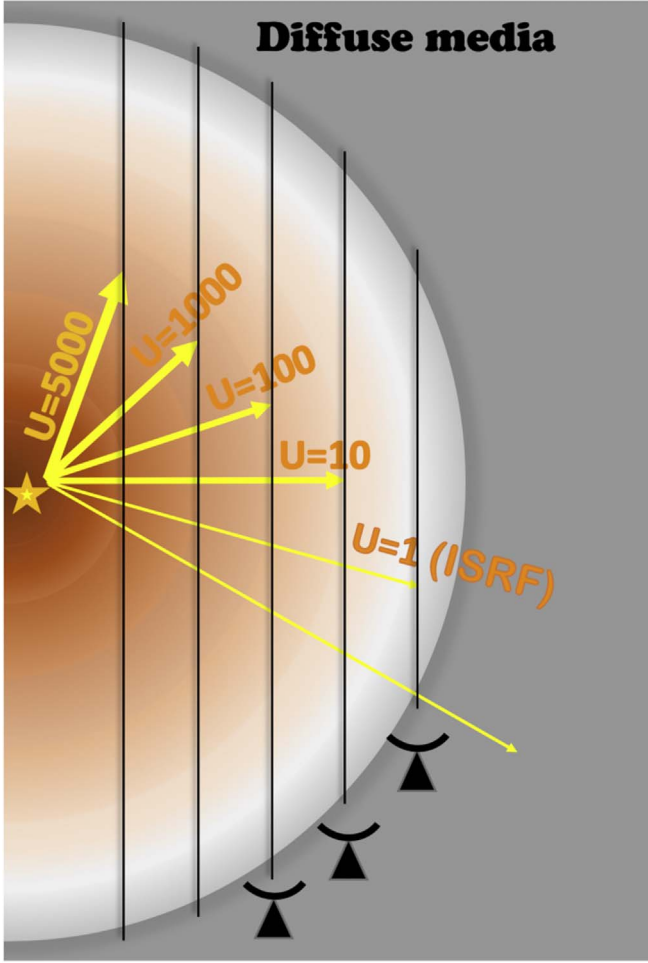
Figure 1. Schematic illustration of a molecular cloud irradiated by a central star. Different lines of sight probe the different average radiation fields, which are characterized by radiation strength U spanning from 5000 to 1.

radiation field of strength $U = 5000$, as illustrated in Figure 1. Other lines of sight more distant from the star probe grains irradiated by weaker radiation fields. Note that the upper value of U is chosen arbitrarily, but it is perhaps typical for photodissociation regions (PDRs).

Let a be the effective size of the irregular grain that is defined as the radius of the equivalent sphere with the same volume as the irregular grain. According to RAT alignment theory, grains are efficiently aligned when they can be spun-up to suprathermal rotation by an anisotropic radiation field.

The radiative torque induced by the interaction of the anisotropic radiation field with the irregular grain is defined by

$$\Gamma_{RAT} = \pi a^2 \gamma u_{rad} \left(\frac{\lambda}{2\pi} \right) Q_\Gamma, \qquad (1)$$

where γ is the anisotropy degree of the radiation field, and Q_Γ is the RAT efficiency. We adopt $\gamma = 0.1$ for the diffuse medium and $\gamma = 0.7$ for MCs (Draine & Weingartner 1996).

Following Lazarian & Hoang (2007), the RAT efficiency can be approximately described by two power laws as follows:

$$\mathbf{Q}_\Gamma \approx 0.4 \left(\frac{\lambda}{1.8a} \right)^{-\eta}, \qquad (2)$$

where $\eta = 0$ for $\lambda/a < 1.8$ and $\eta = 3$ for $\lambda/a \gtrsim 1.8$. This scaling was obtained by approximating numerical calculations with Equations (2) for different grain compositions and grain shapes (Lazarian & Hoang 2007). A slightly shallower slope is obtained from numerical calculations for an extended ensemble of grain shapes by Herranen et al. (2019).

The grain rotation is damped due to collisions with gas species (atoms and molecules) followed by their evaporation and the emission of IR photons after absorption of starlight. Let us define the ratio of the rotational gas damping to IR damping times as $\tau_{gas}/\tau_{em} \equiv F_{IR}$ (see Appendix A). By plugging Γ_{RAT} (Equation 1) into $\omega_{RAT} = \Gamma_{RAT}\tau_{damp}/I$, we can obtain the maximum angular velocity spun-up by RATs,

$$\frac{\omega_{RAT}}{\omega_T} \simeq 48.7 \hat{\rho} a_{-5}^{3.2} U \left(\frac{\gamma}{0.1} \right) \left(\frac{30 \text{ cm}^{-3}}{n_H} \right) \left(\frac{\bar{\lambda}}{1.2\mu m} \right)^{-1.7}$$
$$\times \left(\frac{100 \text{ K}}{T_{gas}} \right) (1 + F_{IR}), \qquad (3)$$

where $a_{-5} \equiv a/(10^{-5} \text{ cm})$, $\hat{\rho} = \rho/(3 \text{ g cm}^{-3})$ where ρ is grain mass density, and F_{IR} is the dimensionless coefficient of rotational damping by IR emission as given by

$$F_{IR} \simeq 0.91 \left(\frac{U^{2/3}}{a_{-5}} \right) \left(\frac{30 \text{ cm}^{-3}}{n_H} \right) \left(\frac{100K}{T_{gas}} \right)^{1/2}, \qquad (4)$$

and the thermal rotation rate ω_T is given by

$$\omega_T = \left(\frac{kT_{gas}}{I} \right)^{1/2} = \left(\frac{15kT_{gas}}{8\pi\alpha_1\rho a^5} \right)^{1/2}$$
$$\simeq 1.6 \times 10^5 T_2^{1/2} a_{-5}^{-5/2} \alpha_1^{-1/2} \text{ rad s}^{-1},$$

where $T_2 = T_{gas}/100$ K, assuming the rotational kinetic energy of a grain around one axis is equal to $kT_{gas}/2$. For simplicity, we assume $\alpha_1 = 1$ throughout the paper. For above analytical estimates, the RAT efficiency averaged over the radiation spectrum $\overline{Q}_\Gamma \approx 2(\bar{\lambda}/a)^{-2.7}$ for $a < \bar{\lambda}/1.8$ has been used (see Equation (68) in Hoang et al. 2014).

Let a_{align} be the critical size that grains can be driven to suprathermal rotation at which $\omega_{RAT}/\omega_T = 3$. Above this limit, the degree of grain alignment starts to rise, and eventually, grains achieve perfect alignment if high-J attractors are present (Hoang & Lazarian 2016). From Equation (3) and the suprathermal rotation criterion, we can calculate the critical size of aligned grains for the various values of U. This alignment size depends on the gas density, temperature, and intensity in the radiation field. The representative results for a few values of U with two different tensile strengths are listed in the Table 2. For the typical ISM, $U = 1$, and one has $a_{align} \sim 0.055 \ \mu m$, and a_{align} becomes smaller for higher values of U.

2.1.2. Grain Alignment Function

Numerical simulations in Hoang & Lazarian (2016) show that if the RAT alignment has a high-J attractor point, then, grains can be perfectly aligned when they are spun-up to suprathermal rotation. For grains without iron inclusions (i.e., ordinary paramagnetic material), high-J attractors are only present for a limited range of the radiation direction that depends on grain shape. This range is
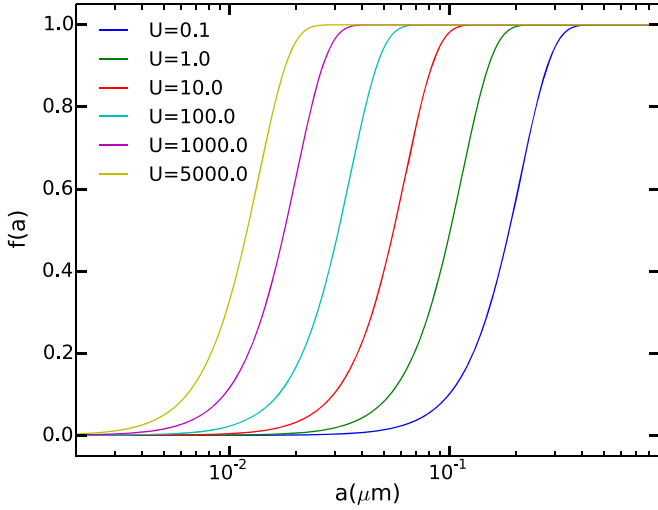
Figure 2. Alignment function $f(a)$ obtained for various radiation strengths U. The alignment function is broader for higher values of U due to the decrease of the alignment size a_{align} with increasing U.

increased if grains have an enhanced magnetic susceptibility by including iron clusters (Lazarian & Hoang 2008; Hoang & Lazarian 2016). For grains smaller than a_{align}, numerical simulations show that the alignment degree is rather small even in the presence of iron inclusions because grains rotate subthermally (Hoang & Lazarian 2016). Thus, to describe the size-dependence of grain alignment degree, we adopt an alignment function

$$f(a) = f_{min} + (f_{max} - f_{min})\left[1 - \exp\left(-\left(\frac{0.5a}{a_{align}}\right)^3\right)\right], \quad (5)$$

where we fix $f_{max} = 1.0$, corresponding to a perfect alignment of large grains. A lower value of f_{min} describes the alignment of small grains of $a < a_{align}$, chosen to be 10^{-3}, so that their contribution to the total polarization is negligible.

The above alignment function approximately agrees with the results obtained from inverse modeling of polarization data from Draine & Fraisse (2009) and Hoang et al. (2014). Therefore, it is appropriate to use this alignment function for modeling dust polarization.

Figure 2 shows the alignment function calculated for different radiation strengths. One can see that the stronger radiation field can align smaller grains, shifting the alignment function toward smaller sizes. In other words, the range of aligned grains becomes broader for higher radiation intensities.

2.2. Grain Rotational Disruption by the RATD Mechanism

2.2.1. Grain Disruption Size and Tensile Strength

A rapidly spinning grain of angular velocity ω develops a tensile stress of $S = \rho\omega^2 a^2/4$ where ρ is the mass density of dust. For large grains in the strong radiation field, the angular velocity by RATs can be sufficiently large such that S exceeds the maximum tensile strength S_{max} of the grain material, resulting in rotational disruption (Hoang et al. 2019).

The critical angular velocity at which the grain is disrupted is given by $S = S_{max}$, which yields

$$\omega_{disr} \simeq \frac{3.6 \times 10^8}{a_{-5}} S_{max,7}^{1/2} \hat{\rho}^{-1/2} \text{ rad s}^{-1}, \quad (6)$$

where $S_{max,7} = S_{max}/(10^7 \text{ erg cm}^{-3})$.

The tensile strength measures the maximal mechanical limit that can resist against an applied tension force before it breaks. The exact value of S_{max} depends on the grain internal structure and composition, which are never constrained for interstellar dust. Physically, compact grains are expected to have higher S_{max} than composite grains due to the difference in the bonding energy between grain constituents. Thus, a higher S_{max} implies a more compact grain, while a lower value of S_{max} implies a porous or composite grain (Hoang 2019b). For instance, polycrystalline bulk solids can have $S_{max} \sim 10^9$–10^{10} erg cm^{-3} (Burke & Silk 1974; Draine & Salpeter 1979), while ideal materials, i.e., diamonds, have $S_{max} \sim 10^{11}$ erg cm^{-3} (see Hoang et al. 2019). In this paper, we assume a reasonable range of tensile strength, $S_{max} \sim 10^6$–10^9 erg cm^{-3}, to account for various structures of interstellar grains. By equating Equations (3) and (6), one can obtain the critical size a_{disr} above which grains are disrupted as follows:

$$\left(\frac{a_{disr}}{0.1 \ \mu m}\right)^{2.7} \simeq 5.1\gamma_{-1}^{-1} U^{-1/3} \bar{\lambda}_{0.5}^{1.7} S_{max,7}^{1/2}, \quad (7)$$

for strong radiation fields of $U \gg 1$ and $a_{max} \leqslant \bar{\lambda}/1.8$, and $\gamma_{-1} = \gamma/0.1$.

The maximum size that grains are still disrupted by RATD is given by (see Hoang & Tram 2019)

$$a_{disr,max} \simeq 1.7\gamma\bar{\lambda}_{0.5}\left(\frac{U}{\hat{n}\hat{T}_{gas}^{1/2}}\right)^{1/2}\left(\frac{1}{1 + F_{IR}}\right)$$
$$\times \hat{\rho}S_{max,7}^{-1/2} \ \mu m, \quad (8)$$

where $\hat{n} = n_H/30$ cm^{-3}, $\hat{T} = T_{gas}/100$ K.

Equation (8) gives $a_{disr,max} \sim 2 \ \mu m$ for the tensile strength of $S_{max} \approx 10^7$ erg cm^{-3}, $\gamma_{rad} = 0.5$, and $\bar{\lambda} = 1.2 \ \mu m$. Therefore, for the diffuse ISM, all grains between a_{disr} and $a_{max} = 1 \ \mu m$ are disrupted. Here, we disregard the possibility of having micron-sized grains in the ISM; therefore, essentially all grains larger than a_{disr} are destroyed by RATD.

Using numerical calculations, we can obtain the critical size of grain alignment (a_{align}) and rotational disruption (a_{disr}) by RATs for various radiation field strengths and local gas properties. Table 2 lists the values of a_{align} and a_{disr} for dust grains in the diffuse ISM illuminated by the different radiation fields. In the typical ISM ($U = 1$), dust grains of size $a \gtrsim 0.06 \ \mu m$ can be aligned by RATs, whereas grains of $a \gtrsim 0.31 \ \mu m$ are disrupted by RATs. In Table 2, we see that both alignment and disruption size become smaller as radiation field strength increases.

2.2.2. Grain Size Distribution in the Presence of RATD

We adopt a mixed dust model consisting of two separate populations of amorphous silicate grains and carbonaceous (graphite) grains (see Weingartner & Draine 2001; Draine & Li 2007). The grain size distribution of component $j = $ sil or gra follows a power-law distribution (Mathis et al. 1977, hereafter MRN):

$$\frac{1}{n_H}\frac{dn_j}{da} = C_j a^{-3.5} \quad \text{at} \quad a_{min} < a < a_{max}, \quad (9)$$

where dn_j is the number density of grains of material j between a, $a + da$, n_H is the number density of hydrogen, and $a_{min} = 10$ Å and $a_{max} = a_{disr}$ are assumed. We take constant C_j from

Weingartner & Draine (2001) for an MRN size distribution as follows: $C_{sil} = 10^{-25.11}$ cm$^{2.5}$ and $C_{gra} = 10^{-25.13}$ cm$^{2.5}$.

The RATD mechanism tends to reduce the abundance of large grains and increases the abundance of smaller grains because of the conservation of total dust mass. To account for this effect, we assume that the slope of the size distribution can be constant and increase the normalization constant C (see more details in Giang et al. 2020).

Previous studies (e.g., Kim & Martin 1995; Draine & Fraisse 2009) show that different grain shapes and axial ratios r can reproduce the observational data. Therefore, we consider two special cases of a prolate spheroidal shape with $r = 1/3$ and an oblate spheroidal shape with $r = 1.5$, for both silicate and carbonaceous grains.

3. Polarization of Starlight

3.1. Polarization Curves

For modeling polarization, we assume that graphite grains are randomly oriented, whereas silicate grains can be aligned via RATs. The polarization of starlight arising from absorption and scattering of aligned silicate grains in a slab of thickness dz is defined as

$$dp_\lambda(x, z) = \frac{1}{2} \int_{a_{align}}^{a_{max}} (C_x - C_y) \frac{dn_{sil}}{da} da dz, \qquad (10)$$

where C_x and C_y are the grain cross sections along the x- and y-axes, respectively, in a reference system in which the line of sight is directed along the z-axis.

Following Hoang et al. (2014), one has

$$C_x - C_y = C_{pol} R \cos^2 \zeta, \qquad (11)$$

where R is the Rayleigh reduction factor (Roberge & Lazarian 1999), and ζ is the angle between the magnetic field and the plane of the sky.

Let $f = R \cos^2 \zeta$ be the effective degree of grain alignment, which depends on the grain size (Hoang & Lazarian 2016). In the following, to explore how the polarization spectrum changes with the local radiation field, we assume that the magnetic field is uniform along the line of sight and lies in the plane of the sky, so $\cos^2 \zeta = 1$. The polarization degree produced by all grains along the line of sight is given by

$$\frac{P_\lambda}{N_H} = \int_{a_{align}}^{a_{max}} \frac{1}{2} C_{pol}^{sil}(\lambda, a) f(a) \frac{1}{n_H} \frac{dn_{sil}}{da} da, \qquad (12)$$

where $N_H = n_H L$ where L is the length of the line of sight.

Equation (12) can be rewritten as

$$P_\lambda = \sigma_{pol}(\lambda) \times N_H, \qquad (13)$$

where σ_{pol} in units of cm^2 H^{-1} is the polarization cross section.

3.2. Numerical Results

To obtain insights into the dependence of the polarization spectrum on grain alignment and disruption, we consider two typical environments, (1) the standard diffuse ISM and (2) dense molecular cloud, using the physical parameters listed in Table 1. We calculate the polarization of starlight using the cross sections C_{pol} and C_{ext} obtained from Guillet et al. (2018), which fit well the average Planck full-sky emission and polarization.

Table 1
Physical Parameters for the Diffuse ISM and Dense MC

Parameters	Diffuse ISM	MC
n_H (cm^{-3})	30	10^4
T_{gas} (K)	100	20
ρ (g cm^{-3})	3	3
γ	0.1	0.7
u_{rad} (erg cm^{-3})	8.64×10^{-13}	Varied
$\bar{\lambda}$ (μm)	1.2	Varied

Figure 3 shows the polarization curves for the diffuse ISM without RATD (left panel) and with RATD (right panel), assuming an axial ratio of grains $r = 1/3$ and tensile strength $S_{max} = 10^7$ erg cm^{-3}.

The left panel of Figure 3 shows that the polarization degree peaks (i.e., maximum polarization) at wavelength $\lambda_{max} \sim 0.48$ μm at $U = 1$ (green dashed line) when RATD is not taken into account. Note that the polarization spectrum at $U = 1$ reflects the results for a typical interstellar radiation field. As the radiation field strength U increases, the peak wavelength moves to shorter wavelengths because of the enhancement of small grains by RATs.

The right panel of Figure 3 shows the results obtained when RATD is taken into account. It shows that the width of the polarization spectrum becomes narrower as the radiation field strength increases. The reason for that is that the stronger radiation field not only makes smaller grains aligned but also disrupts large grains into smaller ones. As a result, the polarization degree at long wavelengths (optical-NIR) decreases, whereas the polarization degree at UV wavelengths increases with increasing U.

Figure 4 is the same as Figure 3 but shows the results for a higher tensile strength $S_{max} = 10^9$ erg cm^{-3}. The results for the case without disruption (left panel) are the same, but the effect of RATD (right panel) is less prominent than the case of the lower tensile strength. Following Equation (7), the grain disruption size by RATD is determined by the tensile strength. The RATD disrupts larger grains when they have a higher tensile strength (see Table 2), and thus, a wider range of aligned grain sizes contributes to the polarization. As a result, the polarization degree is larger, but their profiles remain similar.

Figure 5 shows similar results but for an axial ratio $r = 1.5$. The polarization degree is larger than for the case where $r = 1/3$, but the peak wavelength and shape of the spectrum are similar.

Figure 6 shows the results for a molecular cloud with a central star (see Figure 1) without RATD (left panel) and with RATD (right panel). The polarization degree is, in general, lower than that in the diffuse media (Figure 3) because a high number gas density of MC results in a faster rotational damping such that the critical size of aligned grains is larger. As a result, the maximum polarization degree decreases, and the peak wavelength increases. Nevertheless, the effect of RATD is similar, which acts to decrease the optical-NIR polarization and decreases the UV polarization (see Figure 3, right panel). Figure 7 is the same as Figure 6 but shows the results for a molecular cloud without a star and for a molecular cloud located next to a nearby star.

One can see from the top panels of Figure 7 that the polarization curves have little change in the peak wavelength as the visual
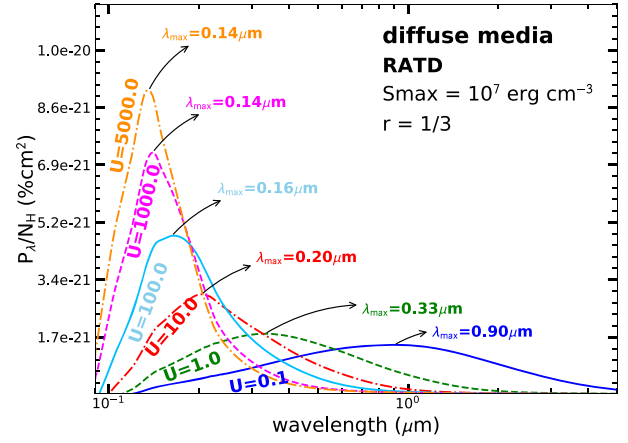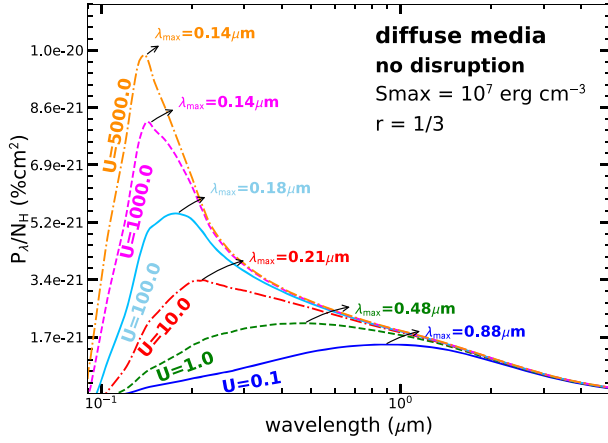
Figure 3. Polarization spectrum due to extinction of starlight by dust grains aligned with axial ratio $r = 1/3$ by RATs in the diffuse media at various radiation field strengths for two cases without RATD (left panel) and with RATD (right panel). The tensile strength $S_{\rm max} = 10^7$ erg cm^{-3} is considered.
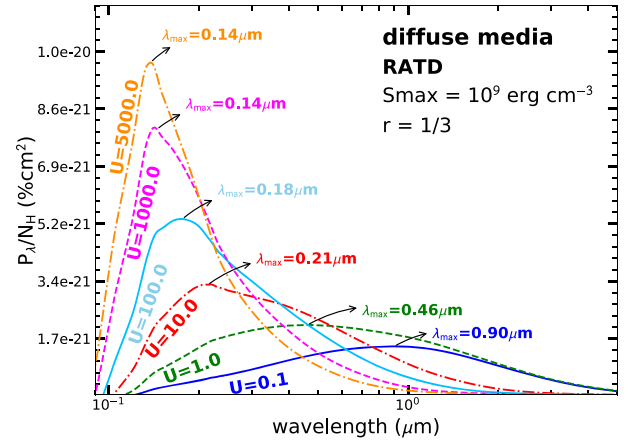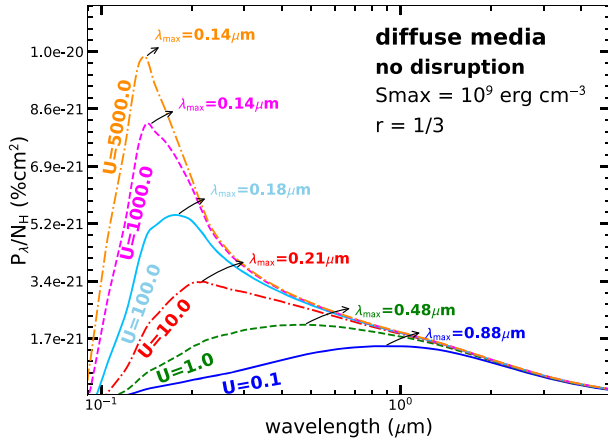

Figure 4. Same as Figure 3, but for a higher tensile strength of $S_{\rm max} = 10^9$ erg cm^{-3}. The effect of RATD is weaker due to the larger tensile strength.

Table 2
Grain Alignment and Disruption Size for the Diffuse Media with $S_{\rm max} = 10^7$ and $S_{\rm max} = 10^9$

| Radiation Strength | Diffuse ISM | | | |
| | $S_{\rm max} = 10^7$ erg cm^{-3} | | $S_{\rm max} = 10^9$ erg cm^{-3} | |
(U)	$a_{\rm align}$ (μm)	$a_{\rm disr}$ (μm)	$a_{\rm align}$ (μm)	$a_{\rm disr}$ (μm)
0.1	0.105	1.0	0.105	1.0
1	0.057	0.31	0.057	1.0
10	0.031	0.15	0.031	0.4
100	0.018	0.10	0.018	0.25
1000	0.010	0.076	0.010	0.18
5000	0.007	0.062	0.007	0.15

extinction increases and is almost same at high A_V, where very weak radiation results in very little disruption of the grains.

We also consider the case where the ambient interstellar radiation field is 10 times stronger than the standard ISRF, such that grains at the outermost region of the cloud in a dense MC are exposed to $U = 10$. The obtained results are shown in the bottom panels of Figure 7. The profile of the polarization spectrum is similar to the top panels, but the polarization degree at longer wavelengths at the outermost region of the cloud becomes smaller when RATD is taken into account (see

right panels of Figure 7). It arises from the fact that large grains at the surface of the molecular cloud can be disrupted into small grains only by a stronger radiation field. However, deep inside the cloud, even the strong interstellar radiation cannot disrupt grains due to dust extinction.

4. Polarized Thermal Emission from Dust Grains

4.1. Polarization Degree

Dust grains heated by starlight re-emit thermal radiation in infrared. For the optically thin regime, the total emission intensity and polarized intensity are, respectively, given by (Draine & Fraisse 2009) as follows:

$$\frac{I_{\rm em}(\lambda)}{N_{\rm H}} = \sum_{j={\rm sil,car}} \int_{a_{\rm min}}^{a_{\rm max}} Q_{\rm ext} \pi a^2$$
$$\times \int dT B_\lambda(T_d) \frac{dP}{dT} \frac{1}{n_{\rm H}} \frac{dn_j}{da} da,$$
$$\frac{I_{\rm pol}(\lambda)}{N_{\rm H}} = \int_{a_{\rm min}}^{a_{\rm max}} f(a) Q_{\rm pol} \pi a^2$$
$$\times \int dT B_\lambda(T_d) \frac{dP}{dT} \frac{1}{n_{\rm H}} \frac{dn_{\rm sil}}{da} da, \quad (14)$$

where dP/dT is the temperature distribution function, which depends on the grain size and radiation strength U, and B_λ is
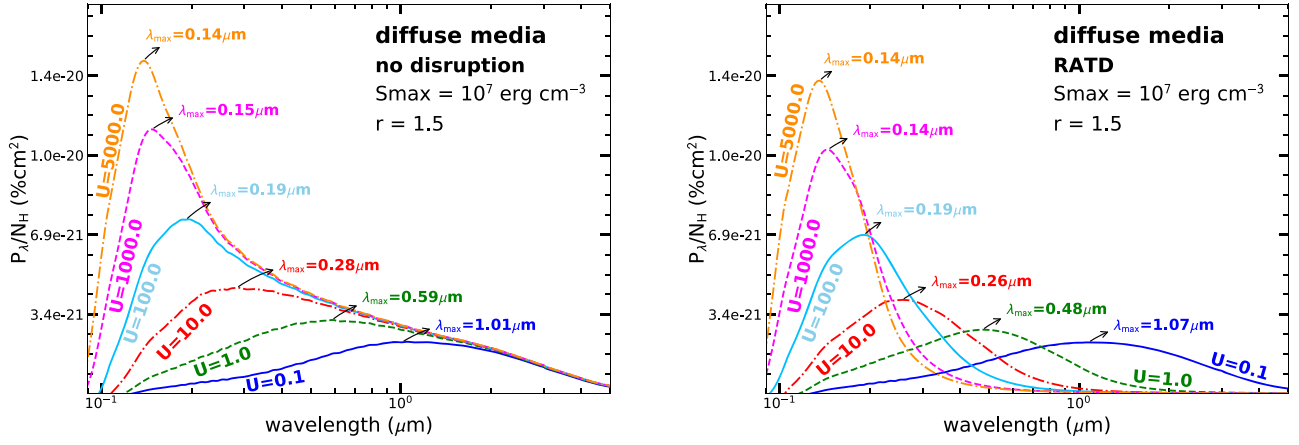
Figure 5. Same as Figure 3, but for oblate grains with axial ratio $r = 1.5$. The polarization degree is higher, but the spectrum is similar.
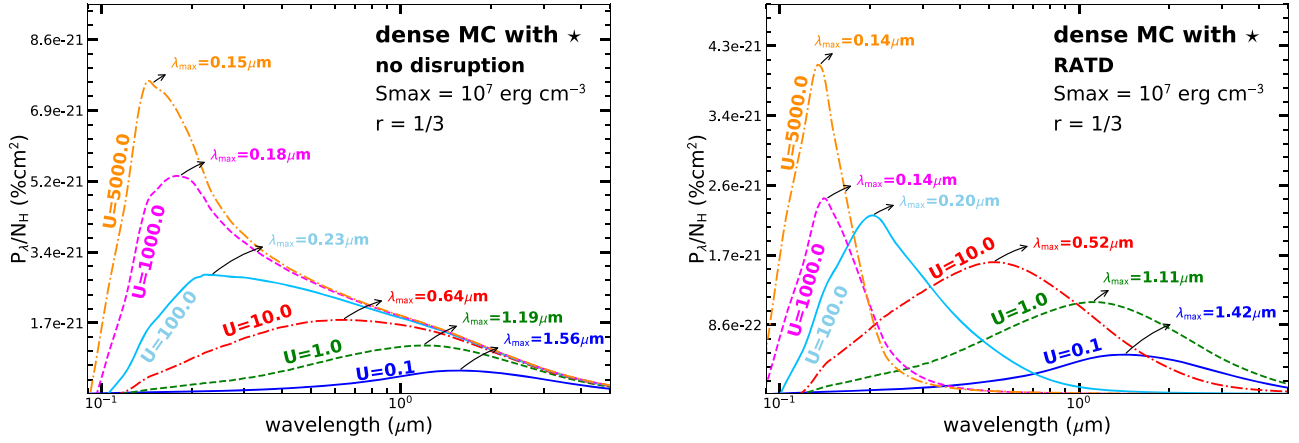

Figure 6. Polarization spectrum due to extinction of starlight by aligned grains in a molecular cloud with a central star. The axial ratio of aligned dust grain is $r = 1/3$, and the tensile strength is $S_{max} = 10^7$ erg cm^{-3}, for the case without RATD (left panel) and with RATD (right panel). The polarization spectrum changes with the radiation strength U.

the Planck function as given by

$$B_\lambda(\lambda, T) = \frac{2hc^2}{\lambda^5} \frac{1}{e^{hc/(kT\lambda)} - 1}. \quad (15)$$

Above, we disregard the minor effect of grain alignment on the thermal emission, which is considered in Draine & Fraisse (2009).

The polarization degree is then given by

$$P(\%) = 100 \times \left(\frac{I_{pol}}{I_{em}} \right). \quad (16)$$

4.2. Grain Temperature Distribution

Dust grains are heated to high temperatures by the absorption of optical/UV photons from stars, and subsequently, the grains cool down by re-emitting photons at long wavelengths. Let dP be the probability of finding the grain temperature in the interval $[T, T + dT]$. Large grains can achieve a steady temperature due to their high heat capacity, but small grains undergo strong temperature fluctuations due to their low heat capacity.

We compute dP/dT using a DustEM code that is publicly available at https://www.ias.u-psud.fr/DUSTEM/. The left panel of Figure 8 shows the temperature distribution function of silicate grains at several sizes and the standard radiation field

($U = 1$). The temperature distribution is very broad for small grains ($a < 0.05\ \mu$m) and becomes narrower for larger grains. The right panel of Figure 8 shows the change in the temperature for silicate grains of size $a = 0.01\ \mu$m subject to various radiation fields. For a low radiation strength of $U < 10$, the temperature distribution is broad, and the distribution becomes narrower and shifts to higher peak temperature as U increases.

4.3. Polarization Spectrum for the Diffuse Interstellar Medium

Figure 9 shows the polarization spectrum of thermal emission from dust grains aligned by RATs in the absence of RATD (left panel) and presence of RATD (right panel) for prolate grains of axial ratio $r = 1/3$, assuming a tensile strength $S_{max} = 10^7$ erg cm^{-3}.

In the absence of RATD (left panel of Figure 9), the maximum polarization degree increases with increasing the radiation strength U as a result of an enhanced alignment of small grains (see Figure 2). The peak wavelength of the polarization spectrum moves toward short wavelengths as U increases, but their spectral profiles remain similar. When the RATD mechanism is taken into account (right panel of Figure 9), the polarization degree for $U \gtrsim 1$ is essentially lower than for the case without RATD due to the removal of large grains by RATD (see Table 2). Moreover, the peak of
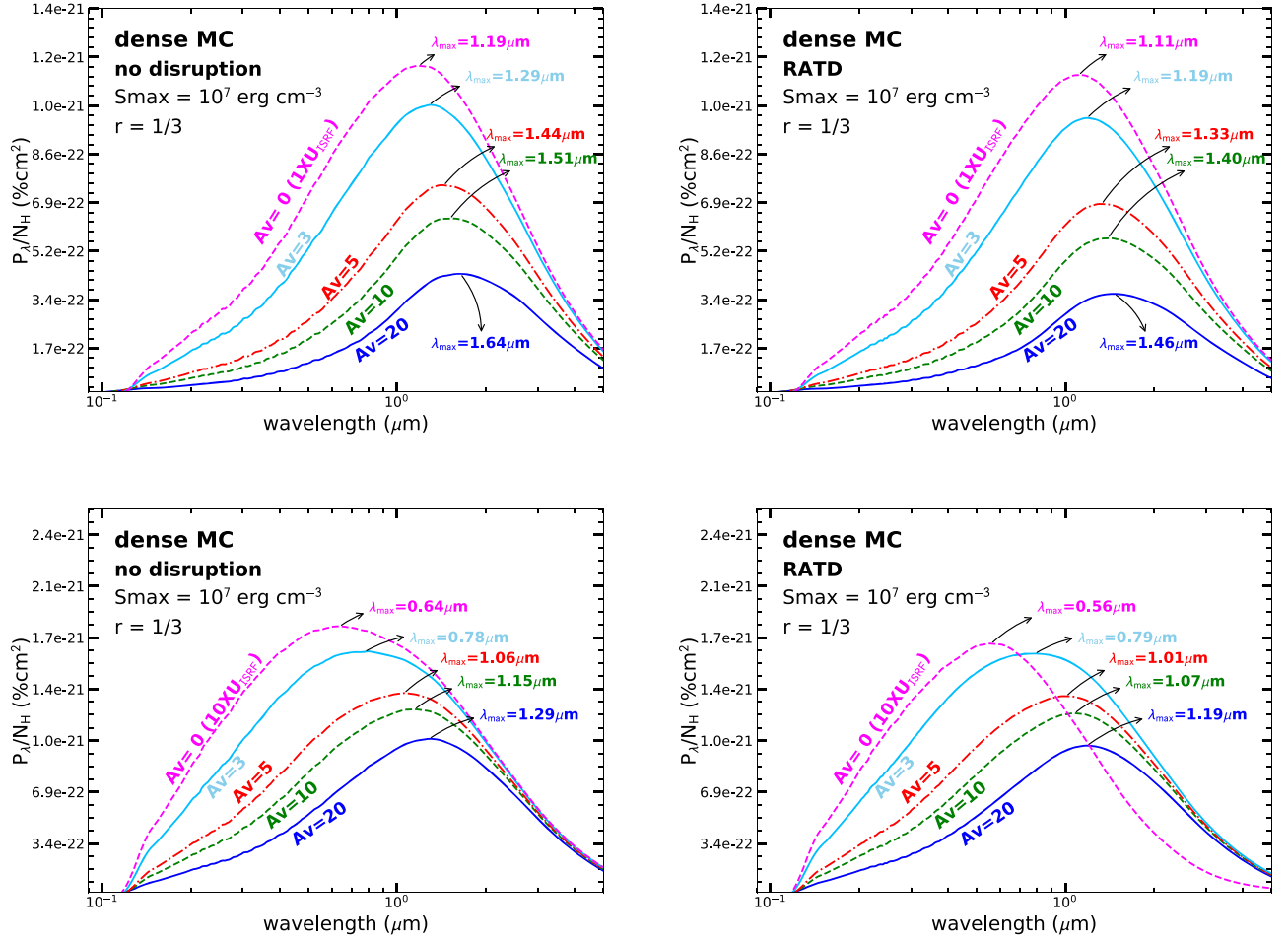
Figure 7. Same as Figure 6, but without a central star in a molecular cloud. We consider a standard ISRF ($1 \times u_{ISRF}$, upper panels) and an ISRF 10 times stronger ($10 \times u_{ISRF}$, bottom panels). Here, A_V is the extinction measured from the cloud surface inward.
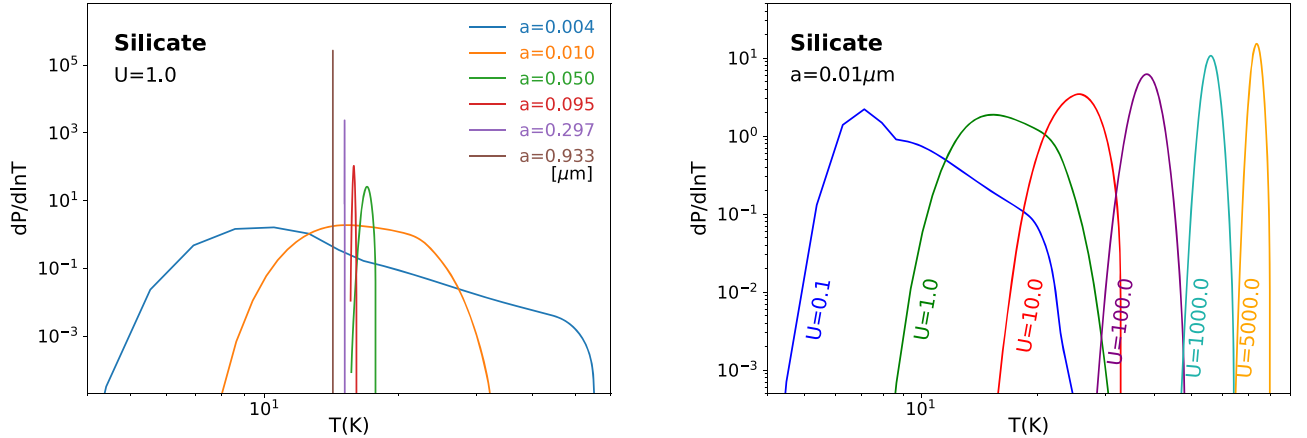

Figure 8. Temperature probability distribution $dP/d\ln T$ for silicate grains at $U = 1$ with various grain sizes (left panel) and at $a \sim 0.01$ μm with $U = 0.1$–5000 (right panel).

polarization degree decreases as the radiation strength increases from $U = 0.1$ (blue line) to $U = 1.0$ (green line).

Figure 10 shows the same results but for dust grains having a higher tensile strength (i.e., $S_{max} = 10^9$ erg cm^{-3}). The results for the case without disruption (left panel) are the same as those of Figure 9. In the presence of RATD (right panel), a similar trend is observed, but the maximum polarization degree increases for $U = 0.1$–1 and then decreases as the radiation strength increases from $U = 1$ to $U = 10$ (red line). The reason

for this is that the disruption requires a higher radiation strength than do grains with lower S_{max}.

Figure 11 shows similar results to Figures 9 but for oblate grains of axial ratio $r = 1.5$. It shows that increasing the axial ratio of grains results in a shorter peak wavelength due to efficient alignment of elongated dust grains, but the shapes of the polarization curves are not influenced strongly, even in the case for which dust grain disruption is taken into account.
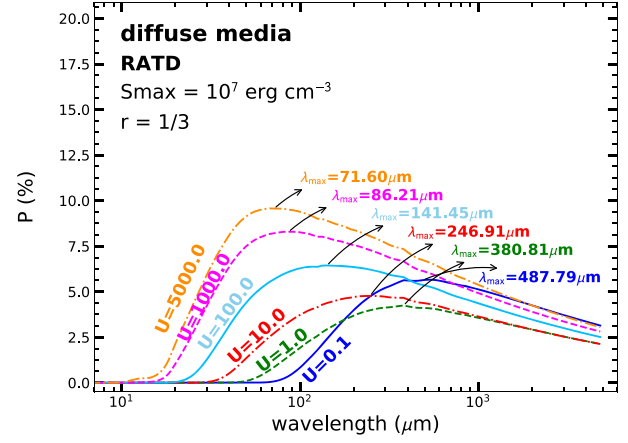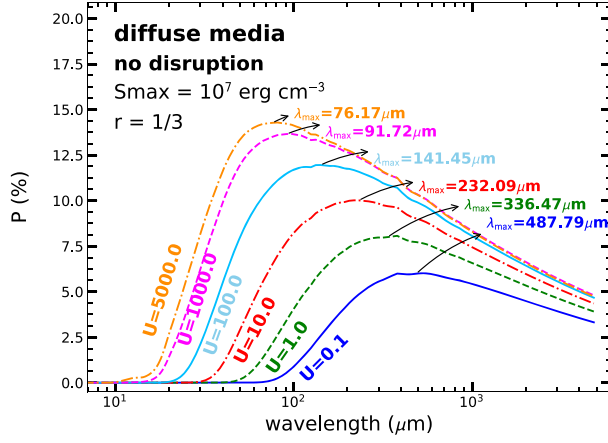
Figure 9. Polarization spectrum of thermal emission from aligned grains by RATs with axial ratio $r = 1/3$ in the diffuse medium at various radiation field strengths, assuming no grain disruption (left panel) and with disruption by RATD (right panel). The tensile strength $S_{\mathrm{max}} = 10^7 \, \mathrm{erg \, cm^{-3}}$ is considered.
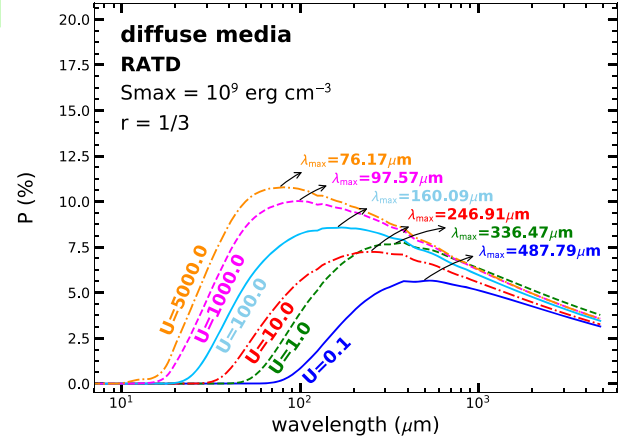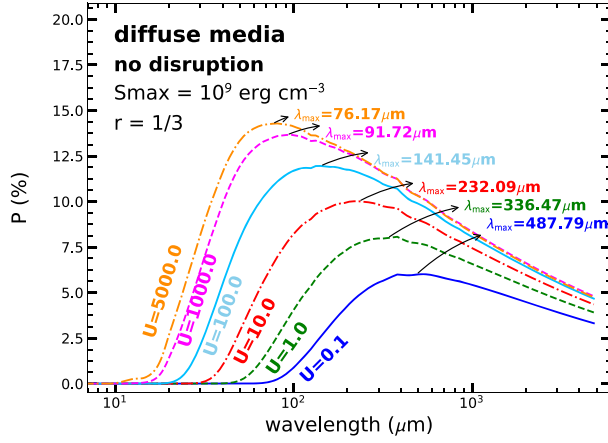

Figure 10. Same as Figure 9, but for a higher tensile strength of $S_{\mathrm{max}} = 10^9 \, \mathrm{erg \, cm^{-3}}$. The polarization degree with RATD is higher due to lower removal of large grains (right panel).
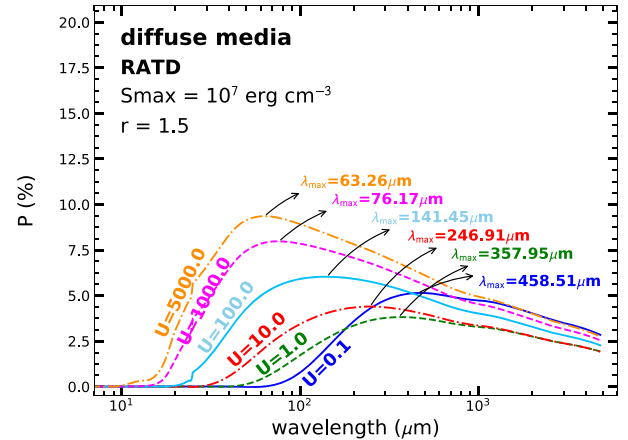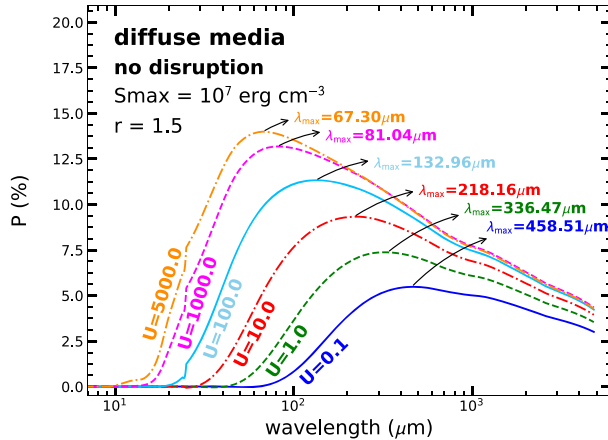

Figure 11. Same as Figure 9, but for oblate grains with axial ratio $r = 1.5$.

4.4. Polarization Spectrum for Molecular Clouds

Figure 12 shows the polarization spectrum obtained for aligned grains in an MC with a central star, assuming $S_{\mathrm{max}} = 10^7 \, \mathrm{erg \, cm^{-3}}$. As can be seen in the right panel of Figure 12, the polarization degree first increases from $U = 0.1$ to $U = 10$, and then, it falls between $U = 10$ and $U = 100$ due to the disruption of large grains via the RATD mechanism.

Note that for MCs of higher gas densities (i.e., faster rotational damping), the rotational disruption occurs at $U \sim 10$ because the required radiation strength must be higher than for the diffuse ISM, assuming the same tensile strength.

Figure 13 shows the polarization spectrum in an MC without a star, assuming $r = 1/3$ and $S_{\mathrm{max}} = 10^7 \, \mathrm{erg \, cm^{-3}}$. The polarization curves have a similar shape, and they exhibit little change in the peak wavelength with higher visual extinction.
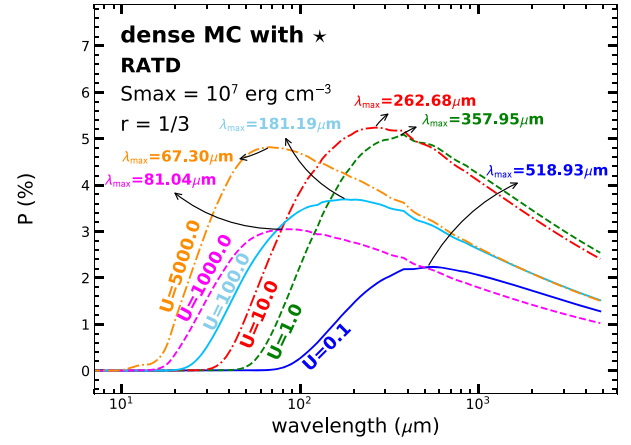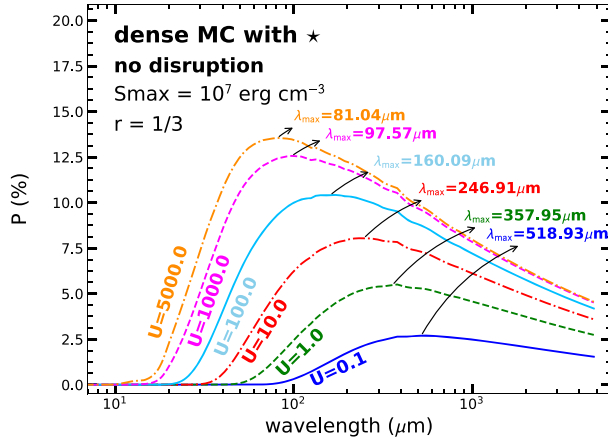
Figure 12. Polarization spectrum of thermal dust emission with axial ratio of $r = 1/3$ and tensile strength of $S_{\max} = 10^7$ erg cm^{-3} in a molecular cloud in which a star is located at its center, for the case without RATD (left panel) and with RATD (right panel). The polarization spectrum changes with the radiation strength U.
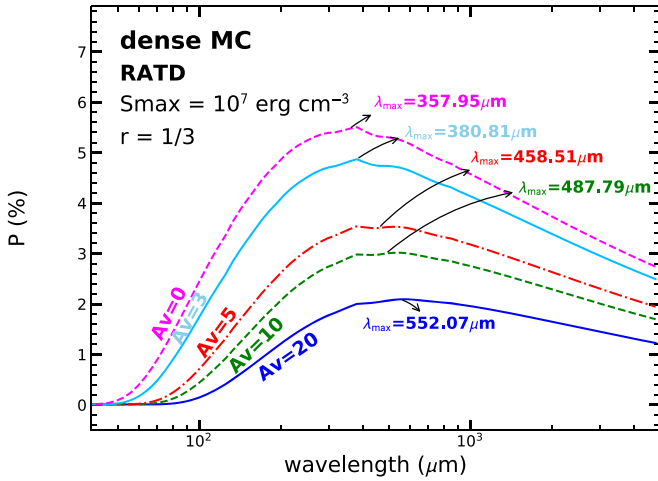

Figure 13. Polarization spectrum due to thermal emission of dust grains with axial ratio of $r = 1/3$ and tensile strength of $S_{\max} = 10^7$ erg cm^{-3} in a molecular cloud without a star. Polarization spectrum changes with different A_V.

For this case, the RATD mechanism is less effective in the polarization spectrum.

4.5. Variation of Submillimeter Polarization with the Radiation Field

To see in more detail how the submillimeter polarization changes with U and grain temperature T_d, we calculate the polarization degree at $\lambda = 850\ \mu$m (P_{850}) using our results from the previous section. Grain temperature is simply estimated from U using the formula $T_d = 16.4a_{-5}^{-1/15}U^{1/6}$ for silicate grains (see Draine 2011).

In the left panel of Figure 14, we show the variation of P_{850} with radiation strength U or grain temperature T_d, calculated for grains in the diffuse ISM and molecular cloud (right panel), assuming a wide range of the tensile strength $S_{\max} = 10^6$–10^9 erg cm^{-3}. The black line shows the results when the RATD is not taken into account. In contrast to the increase of P_{850} with U in the absence of RATD, P_{850} in the diffuse ISM does not change considerably when the radiation strength increases between 1 and 100 when RATD is accounted for. This is because of the compensation of the shift of polarization toward short wavelengths due to lower a_{align} and the increase of

the polarization degree. Indeed, in the case of high tensile strength ($S_{\max} \geqslant 10^8$ erg cm^{-3}), we cannot expect the overall increase of the polarization degree with U but, rather, the variation in the wavelength-dependence polarization. When $U \leqslant 1$ ($T_d < 16.4$ K) for $S_{\max} = 10^9$ erg cm^{-3}, the P_{850} increases as U increases. The peak of P_{850} moves to a smaller radiation strength or lower grain temperature for a smaller $S_{\max}$.

The right panel of Figure 14 shows similar results but for an MC. The amplitude of the polarization variation with U due to RATD is larger for the MC with a central star. Within the RAT paradigm, the wide amplitude of the change for the MC is understood to be due to a high gas number density n_H. The RATD requires a higher radiation strength to be effective. So, in the case of high tensile strength ($S_{\max} \geqslant 10^8$ erg cm^{-3}) for dense MC, when U increases from $U = 0.1$, the polarization degree increases until $U \sim 10$ and then decreases due to RATD. The larger pumping range raises the peak of P_{850}.

The left panel of Figure 15 shows the results for a translucent cloud with gas density between the diffuse ISM and dense MC. A similar trend is observed, but the critical strength where P_{850} starts to decrease is larger than that for the diffuse ISM but smaller than that for the MC. We also study the variation of P_{850} with U for grains with an axial ratio $r = 1.5$ in the right panel and find a similar trend.

5. Discussion

5.1. Physical Forward Modeling of Multiwavelength Polarization

The polarization spectrum closely depends on the grain size distribution and alignment degree of dust grains. Both the grain size and alignment are expected to change with local environments. Inverse modeling of observational data (e.g., Draine & Fraisse 2009; Guillet et al. 2018) is a useful technique to derive the average properties of the dust grains.

In this paper, we focus on the variation of the local radiation strength U and perform forward modeling of multiwavelength dust polarization from UV-optical-NIR (starlight polarization) to far-IR (polarized emission) to predict how the polarization spectrum changes with increasing U from the standard ISRF. We simultaneously treat grain alignment and disruption by RATs. The grain size distribution is modeled consistently using the RATD mechanism, which changes with the strength of the radiation field, as shown in Section 2.1. Our modeling results
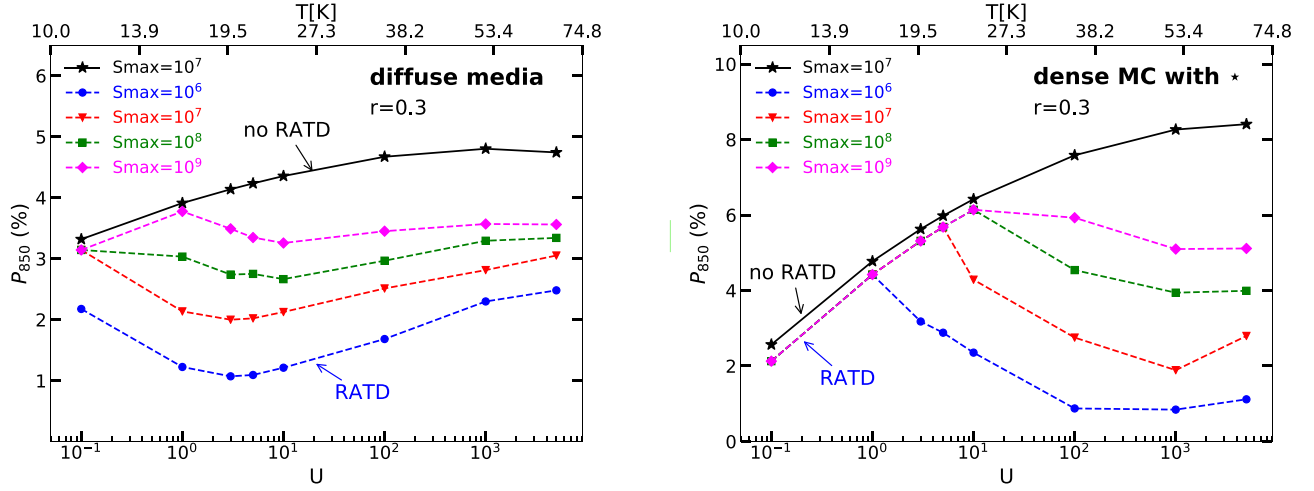
Figure 14. Polarization degree at 850 μm for different radiation strengths (U) or grain temperatures (T_d, top horizontal axis) for two cases, without RATD (black solid line) and with RATD (colored dashed lines), assuming different tensile strengths of grains in the diffuse ISM (left panel) and an MC (right panel). Grains with an axial ratio of $r = 1/3$ are considered.
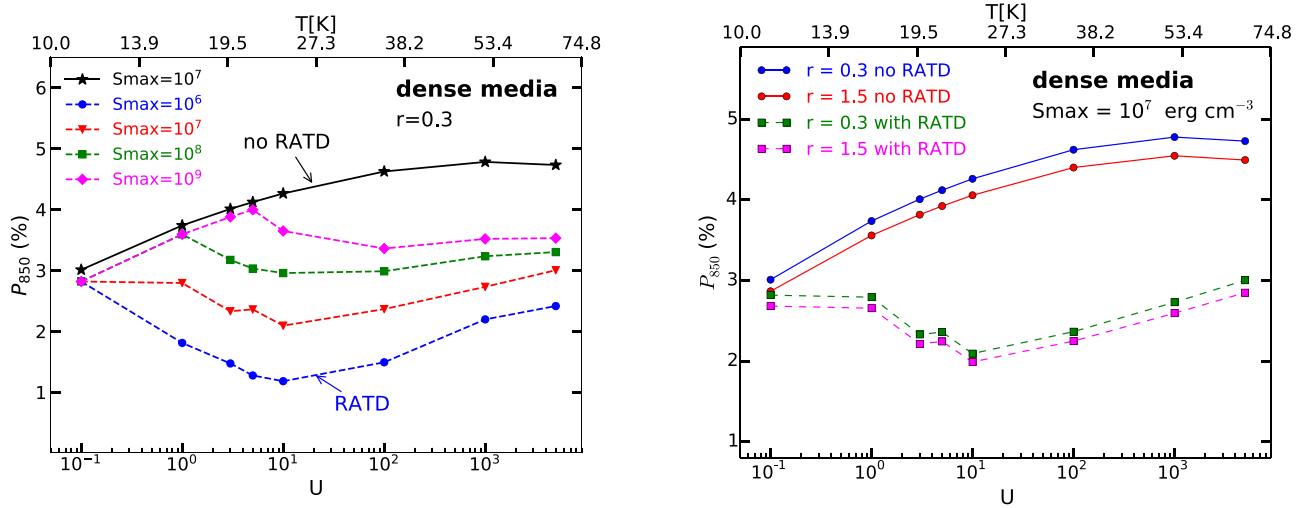

Figure 15. Left panel is the same as Figures 14, but for a translucent cloud with density $n_{\rm H} = 100$ cm^{-3}. The right panel shows the variation of P_{850} for two grain shapes of axial ratio $r = 0.3$ and $r = 1.5$.

show that when the radiation strength U increases, the polarization spectrum, in general, shifts to short wavelengths (see Figures 3–5 for starlight polarization and Figures 9–11 for polarized thermal emission). At the same time, the maximum polarization degree of starlight as well as thermal dust emission also increase with increasing U.

Thanks to the RATD effect, for the first time, we can study the dependence of the interstellar polarization spectrum on the mechanical properties of dust, characterized by the tensile strength $S_{\rm max}$. For a given radiation field, our results show that the polarization spectrum depends crucially on $S_{\rm max}$ because the RATD determines the upper cutoff of the grain size distribution.

Previously, Guillet et al. (2018) modeled the dust polarization spectrum for different local radiation strengths of $U = 0.1$ to $U = 10^3$ using the best-fit alignment function (model D) obtained from fitting the average full-sky Planck data. This model does not take into account the variation of grain alignment efficiency with U. As U increases, the polarization spectrum shifts to short wavelengths, but the peak of polarization degree slightly changes.

5.2. Alignment of Small Grains by RATs

In this paper, we assume that grains are efficiently aligned as long as they rotate suprathermally due to spin-up by RATs. As a result, the alignment of small grains of sizes $a < 0.05$ μm can be perfect if the radiation intensity is sufficiently large (see Figure 2). In the unified model of grain alignment (Hoang & Lazarian 2016), efficient alignment requires grains to have enhanced magnetic susceptibility or inclusion of iron clusters. If small grains do not have iron inclusions, their degree of alignment may not be large if high-J attractors are not present (Hoang & Lazarian 2016). To understand how the alignment of small grains affects polarization spectrum, we fix the alignment degree of small grains to be $f_{\rm align} = 0.1$ for $a < 0.05$ μm if Equation (5) returns higher values. The obtained results for starlight polarization are shown in the upper panels in the Figure 16. Without RATD, polarization at short wavelengths, which are mostly produced by small grains, and $\lambda_{\rm max}$ become saturated for $U > 10$, in contrast to Figure 3 where small grains can be perfectly aligned. When RATD is taken into account, the width of the polarization curve becomes narrower for
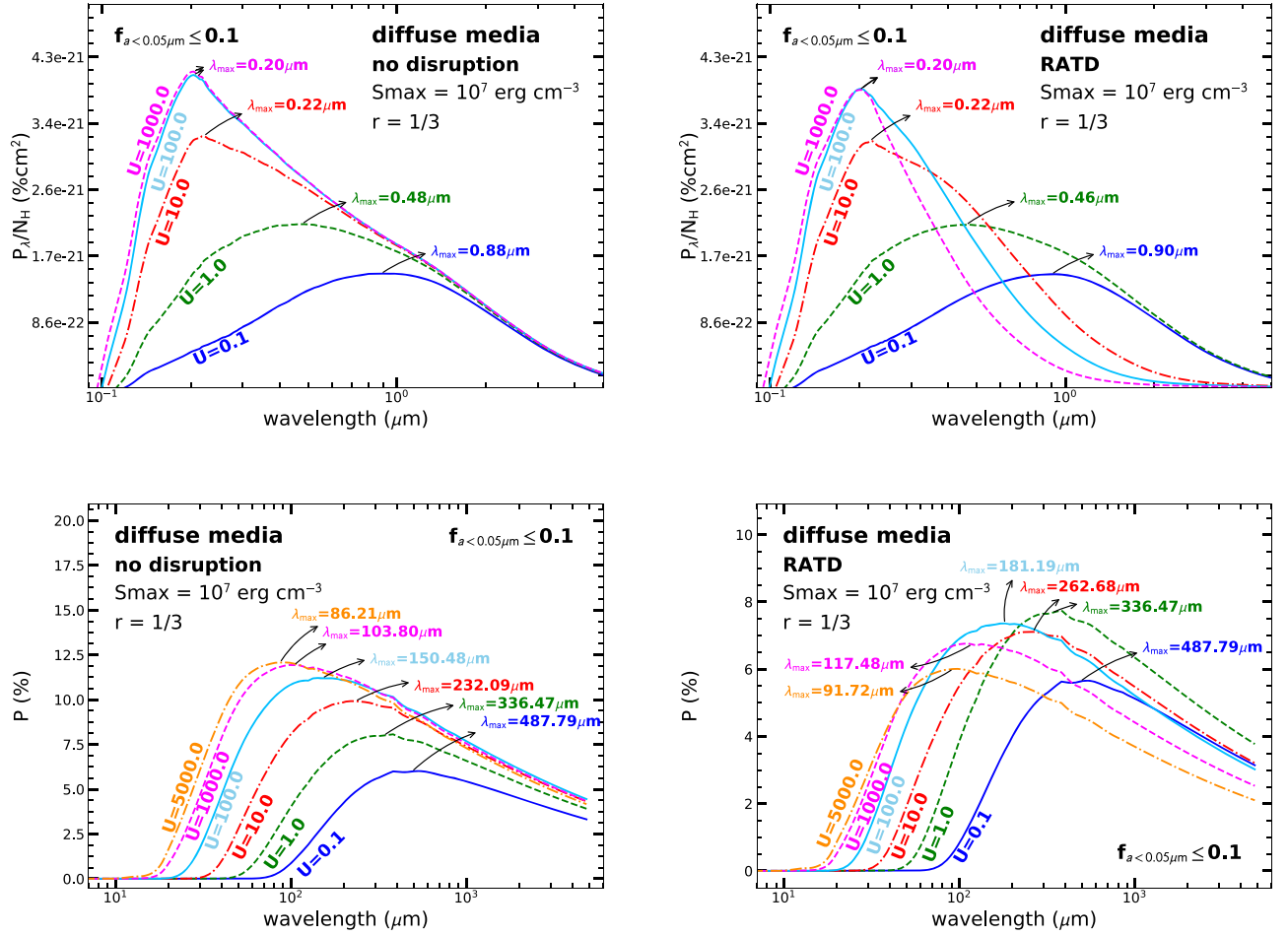
Figure 16. Polarization spectrum due to extinction of starlight by aligned grains (top panels) and thermal emission from aligned grains by RATs (bottom panels) for a grain size distribution in which the alignment degree of small grains (<0.05 μm) is less than 10%. A tensile strength $S_{max} = 10^7$ erg cm^{-3} and axial ratio of 1/3 are assumed.

higher U, but the values of λ_{max} at $U > 10$ do not change. The lower panels of Figure 16 show the spectrum of polarized emission. We can see that the change of the polarization spectrum obtained from dust emission with U is similar to the result in Section 3, but the polarization degree for $U > 10$ is lower. The polarization degree with RATD (lower right panel) decreases for $U > 10$, unlike the result in Section 4 because of the lower alignment degree of small grains.

5.3. Toward Constraining Grain Internal Structures with Observational Data

In Figure 14, we have shown that in the absence of grain disruption by RATD, the polarization degree at 850 μm, denoted by P_{850}, increases monotonically with the radiation intensity (i.e., grain temperature) over the considered range of U. The absence of RATD is equivalent to the situation where grains are made of ideal materials without impurities such that the tensile strength is as high as $S_{max} \sim 10^{11}$ erg cm^{-3} (e.g., diamonds). However, when the RATD effect is taken into account for grains made of weaker materials ($S_{max} \lesssim 10^9$ erg cm^{-3}), the variation of P_{850} with U depends closely on the tensile strength. The general trend is that P_{850} first increases from a low value of U and then decreases when U becomes sufficiently large. The critical value U at the turning point is determined by the value S_{max} and local gas density n_H that controls the grain disruption size a_{disr} according to RATD.

Planck Collaboration et al. (2018) performed a detailed analysis of the variation of P_{850} with the radiation field using Planck data. The authors discovered that P_{850} first increases with increasing grain temperature from $T_d \sim 16$–19 K and then drops as the dust temperature increases to $T_d \gtrsim 19$ K. Such an unusual P_{850}–T_d relationship cannot be reproduced if large grains are not disrupted (i.e., RATD is not taken into account), as shown in Figures 14 and 15. Moreover, the observed trend is, in general, consistent with our model with RATD, but grains have the tensile strength of $S_{max} \lesssim 10^9$ erg cm^{-3}. This range of tensile strength favors a composite internal structure of grains over a compact one.

We also note that the polarization degree of polarized thermal emission obtained from our model is lower than that predicted by Guillet et al. (2018). The difference perhaps arises from the fact that we adopt a power-law size distribution instead of using the best-fit size distribution to the Planck data by Guillet et al. (2018). However, we focus on the overall polarization spectrum with varying radiation strength instead of fitting to the observational data.

5.4. Comparison to the Optical Polarization of SNe Ia

Due to extinction by aligned grains, the starlight is polarized, and the polarization degree varies with the wavelength. In general, the maximum polarization degree is shown at peak wavelength of $\lambda_{max} \sim 0.55$ μm and declines on both sides of

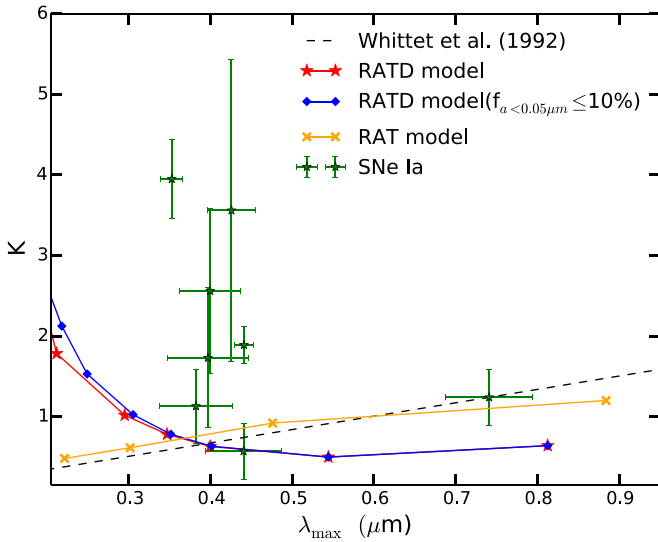**Figure 17.** Extinction sight lines in the λ_{max}–K plane. The orange solid line and the red solid line show the calculation of adopted RAT and RATD, respectively, for dust grains with an S_{max} of 10^7 erg cm^{-3} and axial ratio of $r = 1/3$. The alignment degree of small grains (<0.05 μm) less than 10% is also considered, shown as the blue sold line. The dashed black line traces the relation in Whittet et al. (1992). Points are the observational data: green stars are the samples of SNe Ia from Patat et al. (2015) and Zelaya et al. (2017).

the peak. Following Serkowski (1973), the polarization curve of the starlight can be described by an empirical formula (namely Serkowski law) as follows:

$$P(\lambda) = P_{max} \exp\left(-K \ln^2(\lambda/\lambda_{max})\right) \qquad (17)$$

where P_{max} is the maximum of the polarization degree, λ_{max} is the peak wavelength at P_{max}, and K is a parameter that characterizes the "width" of the polarization profile.

Polarimetric observations of SNe Ia are an excellent test for our theoretical prediction of dust polarization. The polarization curve shows a correlation between Serkowski parameters K and λ_{max}. The "width" parameter K, in Equation (17), is linearly correlated with λ_{max} as $K = c_1 \lambda_{max} + c_2$, where c_1 and c_2 are the average values of the slope and intercept in K–λ_{max} plane. For the standard K–λ_{max} relationship, the current best values for c_1 and c_2 are 1.66 ± 0.09 and 0.01 ± 0.05, respectively (see Whittet 2003). The smaller K shows a broader profile in the polarization curve. The correlation of λ_{max} and K is shown in Figure 17 where the standard relationship by Whittet et al. (1992) is presented by the dashed black line. The left panel of Figure 3 shows a broader curve as the radiation strength increases. From the curve, we calculate λ_{max} and derive the K value by fitting the Serkowski law to the calculated polarization curve. Its correlation is shown as a yellow line in Figure 17. Our calculation for the model of RAT alignment is consistent with the standard relationship. In the right panel of Figure 3, on the other hand, we find that the curve becomes narrower, and λ_{max} gets shorter for higher radiation strengths. This result of the RATD model is consistent with the study of Cikota et al. (2018).

Peculiar polarization data observed toward SNe Ia by Cikota et al. (2018) show that the K parameter does not follow the standard relationship. In order to see if the RATD mechanism can explain SNe Ia polarization data, we calculate the K parameter and λ_{max} using the polarization curves from Section 3. The red line is our samples calculated in

consideration of the RATD mechanism with aligned grains that have axial ratio, $r = 1/3$, at $S_{max} = 10^7$ erg cm^{-3}. A least-squares fit to our samples has slope and intercept $c_1 = -8.5$ and $c_2 = 6.5$. The relationship in our calculation is significantly different from the relation for dust grains in the Taurus region (Whittet et al. 1992), while it is similar to the samples of SNe Ia. The strong radiation from a hot source like SNe Ia can disrupt large grains and form small grains. These small grains are aligned by radiation and produce large K at shorter λ_{max}, representing a negative correlation between K and λ_{max}. We also present the case where the alignment degree of small grains ($a < 0.05$ μm) is less than 10%, by the blue line. This provides a K–λ_{max} relation with a steeper slope at short λ_{max}. This correlation is more comparable to the observational data of SNe.

Finally, our calculations assumed a grain size distribution with a standard slope of $\alpha = -3.5$. In principle, the disruption of large grains by RATD enhances the abundance of small grains, so that the size distribution may be steeper than the standard value as long as RATD occurs (Giang et al. 2020). To see how the slope affects the polarization, we repeat our calculations for $\alpha = -4$. We find that the obtained results are slightly different from the results shown in Figure 3.

6. Summary

In this paper, we have performed physical modeling of multiwavelength polarization by aligned grains for different radiation fields. Our main results are summarized as follows:

1. Using the RAT alignment and RATD theory, we obtain the grain alignment function and size distribution of dust grains for the ISM with various radiation fields and model the polarization of starlight and polarized thermal emission by aligned grains.
2. For the diffuse medium, we find that the polarization spectrum of starlight is shifted toward shorter wavelengths due to the enhancement of small grains when the radiation intensity increases. At the same time, the optical/NIR polarization is reduced due to the disruption of large grains into smaller ones.
3. For polarized thermal emission, we find that the maximum polarization degree increases but the peak wavelength decreases with increasing radiation strength U due to enhanced alignment of small grains. This prediction can be tested with observations such as by SOFIA/HAWC+.
4. In the absence of RATD, we find that the polarization degree at 850 μm (P_{850}) increases with increasing grain temperature (T_d) until $T_d \sim 50$ K. However, when taking into account RATD, we find that the variation of the polarization degree with the radiation strength depends on the tensile strength of the grain materials.
5. Comparing our predictions of P_{850}–T_d with the results from Planck Collaboration et al. (2018) using Planck data, we find that grain disruption must occur in order to reproduce the observed non-monotonic increase of P_{850} with T_d. This suggests that interstellar grains are unlikely to have a compact structure with very high tensile strength but perhaps a composite structure.
6. Based on our results, we suggest that an important way to test RAT theory and RATD is to observe polarization

toward star-forming regions. This is a complementary to the traditional way to test RAT for starless cores.

7. Our models of starlight polarization for high radiation intensity with RATD find that the $K-\lambda_{\max}$ does not follow a standard relationship observed for the average ISRF. However, this predicted trend qualitatively agrees with observations toward SNe Ia.

Appendix A
Grain Rotational Damping

A rotating grain experiences damping due to collisions with gas atoms (i.e., collisional damping) and re-emission of infrared photons after light absorption. The characteristic timescale of grain rotational damping due to gas collisions is

$$\tau_{\text{gas}} = \frac{\pi \alpha_1 \rho a}{3\delta n_{\text{H}}(2\pi m_{\text{H}} k T_{\text{gas}})^{1/2}} \simeq 8.74 \times 10^4$$

$$\times \frac{\alpha_1}{\delta} a_{-5} \hat{\rho} \left(\frac{30 \text{ cm}^{-3}}{n_{\text{H}}}\right) \left(\frac{100 \text{K}}{T_{\text{gas}}}\right)^{1/2} \text{ yr} \qquad (A1)$$

where δ is the drag coefficient of order unity, and α_1 is geometric factor. In general, we expect $\delta \sim \alpha_1$.

Grain rotation also damps due to re-emission of infrared photons on a timescale

$$\tau_{\text{em}} = \frac{8\alpha_1(\beta + 3)}{5} \frac{\zeta(\beta + 4)}{\zeta(\beta + 3)} \frac{\rho a^3}{\hbar^2 c u_{\text{rad}} \langle Q_{\text{abs}} \rangle}$$

$$= 1.60 \times 10^5 \times \frac{\alpha_1 a_{-5}^3 \rho_3}{\langle Q_{\text{abs}} \rangle} \left(\frac{u_{\text{ISRF}}}{u_{\text{rad}}}\right) \left(\frac{T_d}{18 \text{ K}}\right)^2 \text{ yr} \qquad (A2)$$

where $\zeta(x)$ denotes the Riemann ζ-function and Q_{abs} is absorption efficiency factor defined as

$$\langle Q_{\text{abs}} \rangle \equiv \frac{1}{u_{\text{rad}}} \int u_\lambda Q_{\text{abs}}(\lambda) d\lambda. \qquad (A3)$$

The total rate of rotational damping, τ_{damp}, by gas collisions and thermal emission can be written as

$$\tau_{\text{damp}}^{-1} = \tau_{\text{gas}}^{-1} + \tau_{\text{em}}^{-1} = \tau_{\text{gas}}^{-1}(1 + F_{\text{IR}}), \qquad (A4)$$

where $F_{\text{IR}} = \tau_{\text{gas}}/\tau_{\text{em}}$.

Appendix B
Grain Cross Section

Let us consider an oblate spheroidal grain with the symmetry axis a_1 having an effective size a, which is the size of an equivalent sphere of the same volume as the grain. A perfectly polarized electromagnetic wave with the electric field vector E is assumed to propagate along the line of sight. Let $C_{\text{ext}}(E \perp a_1)$

and $C_{\text{ext}}(E \| a_1)$ be the extinction of radiation by the grain for the cases in which E is parallel and perpendicular to a_1, respectively, as a result of light absorption plus scattering. For the sake of simplification, we denote these extinction cross sections by $C_\perp$ and $C_\|$.

For the general case in which E makes an angle θ with a_1, the extinction cross section becomes

$$C_{\text{ext}} = \cos^2 \theta C_\| + \sin^2 \theta C_\perp \qquad (B1)$$

where $C_\perp$ and $C_\|$ denote the extinction of radiation for the cases in which the electric field $\mathbf{E}$ is perpendicular and parallel to symmetry axis $\mathbf{a}$, respectively.

Since the original starlight is unpolarized, one can compute the total extinction cross section for a randomly oriented grain by integrating Equation (B1) over the isotropic distribution of θ, i.e., $f_{\text{iso}} d\theta \sim \sin\theta d\theta$. As a result,

$$C_{\text{ext}} = \frac{1}{3}(2C_\perp + C_\|). \qquad (B2)$$

For dust grains spinning around the principal axis $\mathbf{a}$, the polarization cross sections are

$$C_{\text{pol}} = \frac{C_{\perp,\text{ext}} - C_{\|,\text{ext}}}{2} \text{ for prolates}$$

$$C_{\text{pol}} = C_{\perp,\text{ext}} - C_{\|,\text{ext}} \text{ for oblates.} \qquad (B3)$$

Usually, the grain cross section C is represented through efficiency Q as follows:

$$Q_j \equiv \frac{C_j}{\pi a^2} \qquad (B4)$$

where $j = \text{ext, abs, sca}$ for extinction, scattering, and absorption, respectively.

Appendix C
Extinction and Polarization of Starlight

The extinction of a background star induced by randomly oriented grains in an intervening cloud in units of magnitude is defined by

$$A(\lambda) = 2.5 \log_{10}\left(\frac{F_\lambda^{\text{obs}}}{F_\lambda^\star}\right) = 1.086\tau_\lambda,$$

$$= 1.086 \int \sum_{j=\text{carb,sil}} \sum_{i=0}^{N_a-1} C_{\text{ext}}^j(a_i) n^j(a_i) dz, \qquad (C1)$$

where $F_\lambda^\star$ is the intrinsic flux from the star, $F_\lambda^{\text{obs}} = F_\lambda^\star e^{-\tau_\lambda}$ is the observed flux, τ_λ is the optical depth, and the integration is performed along the line of sight.

To find the polarization by aligned grains, let us define an observer's reference system in which the line of sight is directed along the z-axis, and the x- and y-axes constitute the sky plane. The polarization of starlight arising from the dichroic extinction by aligned grains in a cell of dz is computed as

$$dp(\lambda) = \frac{d\tau_x - d\tau_y}{2} = \sum_{i=0}^{N_a-1} \frac{1}{2}(C_x - C_y)n(a_i)dz, \qquad (C2)$$

where N_a is the number of size bin, $n(a_i) \equiv (dn/da)da$ is the number of grains of size a_i, C_x and C_y are the grain cross section along the x- and y-axes, respectively.

For the case of perfect internal alignment of grain symmetry axis a_1 with angular momentum J, by transforming the grain coordinate system to the observer's reference system and taking corresponding weights, we obtain

$$C_x = C_\perp - \frac{C_{pol}}{2}\sin^2\beta, \tag{C3}$$

$$C_y = C_\perp - \frac{C_{pol}}{2}(2\cos^2\beta\cos^2\zeta + \sin^2\beta\sin^2\zeta), \tag{C4}$$

where ζ is the angle between the magnetic field B and the sky plane and β is the angle between J and B.

The polarization efficiency then becomes

$$C_x - C_y = C_{pol}\frac{(3\cos^2\beta - 1)}{2}\cos^2\zeta. \tag{C5}$$

Taking the average of $C_x - C_y$ over the distribution of the alignment angle β, it yields

$$C_x - C_y = C_{pol}Q_J\cos^2\zeta, \tag{C6}$$

where $Q_J = \langle G_J \rangle$ is the ensemble average of $G_J = (3\cos^2\beta - 1)/2$ that describes the alignment of J and B.

When the internal alignment is not perfect, following the similar procedure, we obtain

$$C_x - C_y = C_{pol}\langle G_J G_X \rangle\cos^2\gamma \equiv C_{pol}R\cos^2\zeta, \tag{C7}$$

where $G_X = (3\cos^2\theta - 1)/2$ with θ being the angle between a_1 and J, and $R = \langle G_J G_X \rangle$ is the Rayleigh reduction factor (see also Roberge & Lazarian 1999). The degree of internal alignment is described by $Q_X = \langle G_X \rangle$.

For a perpendicular magnetic field, i.e., B lies on the sky plane, Equation (B3) simply becomes $C_x - C_y = C_{pol}R$. For an arbitrary magnetic field geometry, let $f = R\cos^2\gamma$ be the effective degree of grain alignment, which is a function of grain size a. Thus, in the following, $f(a)$ is referred as the alignment function.

Plugging the above equation into Equation (C2) and integrating along the line of sight, we obtain

$$p(\lambda) = \int_{a_{align}}^{a_{max}}\sum_{j=carb,sil}\frac{1}{2}C_{pol}^j f^j(a)\frac{dn}{da}da \tag{C8}$$

where $f^j(a_i)$ is the effective degree of grain alignment for the grain specie j of size a_i.

It is more convenient to represent the extinction (polarization) through the extinction (polarization) cross section. Hence, the above equations can be rewritten as

$$A(\lambda) = 1.086\ \sigma_{ext}(\lambda) \times N_H, \tag{C9}$$

$$p(\lambda) = \sigma_{pol}(\lambda) \times N_H \tag{C10}$$

where $N_H(\text{cm}^{-2})$ is the column density, and σ_{ext} and σ_{pol} in units of $\text{cm}^2\,\text{H}^{-1}$ are the dust extinction cross section and polarization cross section, respectively.

ORCID iDs

Thiem Hoang ⓘ https://orcid.org/0000-0003-2017-0982
Jungyeon Cho ⓘ https://orcid.org/0000-0003-1725-4376

References

Alves, F. O., Frau, P., Girart, J. M., et al. 2014, A&A, 569, L1
Andersson, B.-G. 2015, in Magnetic Fields in Diffuse Media, ed. A. Lazarian, E. M. de Gouveia Dal Pino, & C. Melioli (Berlin: Springer), 59
Andersson, B.-G., Lazarian, A., & Vaillancourt, J. E. 2015, ARA&A, 53, 501
Andersson, B.-G., Pintado, O., Potter, S. B., Straižys, V., & Charcos-Llorens, M. 2011, A&A, 534, 19
Burke, J. R., & Silk, J. 1974, ApJ, 190, 1
Cho, J., & Lazarian, A. 2005, ApJ, 631, 361
Cikota, A., Hoang, T., Taubenberger, S., et al. 2018, A&A, 615, 42
Crutcher, R. M. 2012, ARA&A, 50, 29
Dolginov, A. Z., & Mitrofanov, I. G. 1976, Ap&SS, 43, 257
Draine, B. T. 2011, Physics of the Interstellar and Intergalactic Medium (Princeton, NJ: Princeton Univ. Press)
Draine, B. T., & Fraisse, A. A. 2009, ApJ, 696, 1
Draine, B. T., & Li, A. 2007, ApJ, 657, 810
Draine, B. T., & Salpeter, E. E. 1979, ApJ, 231, 77
Draine, B. T., & Weingartner, J. C. 1996, ApJ, 470, 551
Draine, B. T., & Weingartner, J. C. 1997, ApJ, 480, 633
Giang, N. C., Hoang, T., & Tram, L. N. 2020, ApJ, 888, 93G
Guillet, V., Fanciullo, L., Verstraete, L., et al. 2018, A&A, 610, 16
Hall, J. S. 1949, Sci, 109, 166
Herranen, J., Lazarian, A., & Hoang, T. 2019, ApJ, 878, 96
Hildebrand, R. H. 1989, in IAU Symp. 135, Interstellar Dust, ed. L. J. Allamandola & A. G. G. M. Tielens (Dordrecht: Kluwer), 275
Hiltner, W. A. 1949, Natur, 163, 283
Hirashita, H., & Yan, H. 2009, MNRAS, 394, 1061
Hoang, T. 2019a, ApJ, 836, 13
Hoang, T. 2019b, ApJ, 876, 13
Hoang, T., & Lazarian, A. 2008, MNRAS, 388, 117
Hoang, T., & Lazarian, A. 2009a, ApJ, 695, 1457
Hoang, T., & Lazarian, A. 2009b, ApJ, 697, 1316
Hoang, T., & Lazarian, A. 2014, MNRAS, 438, 680
Hoang, T., & Lazarian, A. 2016, ApJ, 831, 159
Hoang, T., Lazarian, A., & Andersson, B.-G. 2015, MNRAS, 448, 1178
Hoang, T., Lazarian, A., & Martin, P. G. 2014, ApJ, 790, 6
Hoang, T., Lazarian, A., & Schlickeiser, R. 2012, ApJ, 747, 54
Hoang, T., & Tram, L. N. 2019, ApJ, 877, 36
Hoang, T., Tram, L. N., Lee, H., & Ahn, S. 2019, NatAs, 3, 766
Jones, A. P., Tielens, A. G. G. M., & Hollenbach, D. J. 1996, ApJ, 469, 740
Jones, T. J., Bagley, M., Krejny, M., Anderson, B.-G., & Bastien, P. 2015, ApJ, 149, 31
Kim, S. H., & Martin, P. 1995, ApJ, 444, 293
Lazarian, A. 2007, JQSRT, 106, 225
Lai, S.-P., Girart, J. M., & Crutcher, R. M. 2003, ApJ, 598, 392
Lazarian, A., Andersson, B.-G., & Hoang, T. 2015, in Polarimetry of Stars and Planetary Systems, ed. L. Kolokolova, J. Hough, & A.-C. Levasseur-Regourd (New York: Cambridge Univ. Press), 81
Lazarian, A., & Finkbeiner, D. 2003, NewAR, 47, 1107
Lazarian, A., & Hoang, T. 2007, MNRAS, 378, 910
Lazarian, A., & Hoang, T. 2008, ApJL, 676, L25
Lazarian, A., & Hoang, T. 2019, ApJ, 883, 122
Mathis, J. S., Mezger, P. G., & Panagia, N. 1983, A&A, 128, 212
Mathis, J. S., Rumpl, W., & Nordsieck, K. H. s. 1977, ApJ, 217, 425M
Patat, F., Taubenberger, S., Cox, N. L. J., et al. 2015, A&A, 577, A53
Planck Collaboration, Ade, P. A. R., Aghanim, N., et al. 2016, A&A, 586, A14
Planck Collaboration, Aghanim, N., Akrami, Y., et al. 2018, arXiv:1807.06212
Purcell, E. M. 1979, ApJ, 231, 404
Roberge, W. G., & Lazarian, A. 1999, MNRAS, 305, 615
Serkowski, K. 1973, in IAU Symp. 52, Interstellar Dust and Related Topics, ed. J. M. Greenberg & H. C. van de Hulst (Dordrecht: Kluwer), 145
Tielens, A. G. G. M., McKee, C. F., & Seab, C. G. 1994, ApJ, 431, 321
Weingartner, J. C., & Draine, B. T. 2001, ApJ, 548, 296
Whittet, D. C. B. 2003, Dust in the Galactic Environment (Bristol: IOP Publishing)
Whittet, D. C. B., Hough, J. H., Lazarian, A., & Hoang, T. 2008, ApJ, 674, 304
Whittet, D. C. B., Martin, P. G., Hough, J. H., et al. 1992, ApJ, 386, 562
Yan, H., Lazarian, A., & Draine, B. T. 2004, ApJ, 616, 895
Zelaya, P., Clocchiatti, A., Baade, D., et al. 2017, ApJ, 836, 88
Zhukovska, S., Henning, T., & Dobbs, C. 2018, ApJ, 857, 94